7. H. Huang, S. C. Yin, L. F. Nazar, *Electrochem. Solid-State Lett.* **4**, A170–A172 (2001).
8. E. S. Takeuchi *et al.*, *Chem. Mater.* **21**, 4934–4939 (2009).
9. E. S. Takeuchi *et al.*, *J. Solid State Chem.* **200**, 232–240 (2013).
10. E. S. Takeuchi *et al.*, *Energy Environ. Sci.* **6**, 1465–1470 (2013).
11. F. Sauvage, V. Bodenez, J. M. Tarascon, K. R. Poeppelmeier, *Inorg. Chem.* **49**, 6461–6467 (2010).
12. K. C. Kirshenbaum *et al.*, *Phys. Chem. Chem. Phys.* **16**, 9138–9147 (2014).
13. J. Rijssenbeek *et al.*, *J. Power Sources* **196**, 2332–2339 (2011).
14. M. Ebner, F. Marone, M. Stampanoni, V. Wood, *Science* **342**, 716–720 (2013).
15. D. C. Bock, K. J. Takeuchi, A. C. Marschilok, E. S. Takeuchi, *Dalton Trans.* **42**, 13981–13989 (2013).
16. A. C. Marschilok *et al.*, *J. Power Sources* **195**, 6839–6846 (2010).
17. R. A. Leising, W. C. Thiebolt, E. S. Takeuchi, *Inorg. Chem.* **33**, 5733–5740 (1994).
18. F. Sauvage *et al.*, *Inorg. Chem.* **47**, 8464–8472 (2008).
19. S. Calvin, in *XAFS for Everyone* (CRC Press, Boca Raton, FL, 2013), p. xxvi.
20. C. J. Patridge *et al.*, *J. Phys. Chem. C* **115**, 14437–14447 (2011).
21. P. Chaurand *et al.*, *J. Phys. Chem. B* **111**, 5101–5110 (2007).
22. J. Wong, F. W. Lytle, R. P. Messmer, D. H. Maylotte, *Phys. Rev. B* **30**, 5596–5610 (1984).
23. P. E. Stallworth, S. Kostov, M. L. denBoer, S. G. Greenbaum, C. Lampe-Onnerud, *J. Appl. Phys.* **83**, 1247–1255 (1998).

MATERIALS SCIENCE

Assembly of micro/nanomaterials into complex, three-dimensional architectures by compressive buckling

Sheng Xu,[1]* Zheng Yan,[1]* Kyung-In Jang,[1] Wen Huang,[2] Haoran Fu,[3,4] Jeonghyun Kim,[1,5] Zijun Wei,[1] Matthew Flavin,[1] Joselle McCracken,[6] Renhan Wang,[1] Adina Badea,[6] Yuhao Liu,[1] Dongqing Xiao,[6] Guoyan Zhou,[3,7] Jungwoo Lee,[1,5] Ha Uk Chung,[1] Huanyu Cheng,[1,3] Wen Ren,[6] Anthony Banks,[1] Xiuling Li,[2] Ungyu Paik,[5] Ralph G. Nuzzo,[1,6] Yonggang Huang,[3]† Yihui Zhang,[3,8]† John A. Rogers[1,2,6,9]†

Complex three-dimensional (3D) structures in biology (e.g., cytoskeletal webs, neural circuits, and vasculature networks) form naturally to provide essential functions in even the most basic forms of life. Compelling opportunities exist for analogous 3D architectures in human-made devices, but design options are constrained by existing capabilities in materials growth and assembly. We report routes to previously inaccessible classes of 3D constructs in advanced materials, including device-grade silicon. The schemes involve geometric transformation of 2D micro/nanostructures into extended 3D layouts by compressive buckling. Demonstrations include experimental and theoretical studies of more than 40 representative geometries, from single and multiple helices, toroids, and conical spirals to structures that resemble spherical baskets, cuboid cages, starbursts, flowers, scaffolds, fences, and frameworks, each with single- and/or multiple-level configurations.

Controlled formation of 3D functional meso-structures is a topic of broad and increasing interest, particularly in the past decade (*1–9*). Uses of such structures have been envisioned in nearly every type of micro/nanosystem technology, including biomedical devices (*10–12*), microelectromechanical components (*13, 14*), photonics and optoelectronics (*15–17*), metamaterials (*16, 18–21*), electronics (*22, 23*), and energy storage (*24, 25*). Although volumetric optical exposures (*4, 6, 19*), fluidic self-assembly (*3, 26, 27*), residual stress-induced bending (*1, 13, 21, 28–31*), and templated growth (*7, 8, 32*) can be used to realize certain classes of structures in certain types of materials, techniques that rely on rastering of fluid nozzles or focused beams of light provide the greatest versatility in design (*5, 6*). The applicability of these latter methods, however, only extends directly to materials that can be formulated as inks or patterned by exposure to light or other energy sources, and indirectly to those that can be depo-sited onto or into sacrificial 3D structures formed with these materials (*5, 6, 18, 19*). Integration of more than one type of any material into a single structure can be challenging. Furthermore, the serial nature of these processes sets practical constraints on operating speeds and overall addressable areas. These and other limitations stand in stark contrast with the exceptional fabrication capabilities that exist for the types of planar micro/nanodevices that are ubiquitous in state-of-the-art semiconductor technologies. Routes to 3D mesostructures that exploit this existing base of competencies can provide options in high-performance function that would otherwise be unobtainable.

Methods based on residual stress-induced bending are naturally compatible with modern planar technologies, and they offer yields and throughputs necessary for practical applications. Such schemes provide access to only certain classes of geometries, through either rotations of rigid plates to yield tilted panels, rectangular cuboids, pyramids, or other hollow polyhedra, or rolling motions of flexible films to form tubes, scrolls, or related shapes with cylindrical symmetry [for reviews, see (*1, 9, 13*)]. Here, we present a different set of concepts in which strain relaxation in an elastomeric substrate simultaneously imparts forces at a collection of lithographically controlled locations on the surfaces of planar precursor structures. The resulting processes of controlled, compressive buckling induce rapid, large-area geometric extension into the third dimension, capable of transforming the most advanced functional materials and planar microsystems into mechanically tunable 3D forms with broad geometric diversity.

As a simple illustrative example, we present results of finite-element analyses (FEAs) (*33*) of the steps for assembly of a pair of 3D conical helices made of monocrystalline silicon in Fig. 1A. The process begins with planar micro/nanofabrication of 2D filamentary serpentine silicon ribbons (2 μm thick, 60 μm wide), with spatial gradients in their arc radii. Lithographically defined exposure of these structures to ozone formed using ultraviolet light creates precisely controlled patterns of surface hydroxyl terminations at strategic locations (red dots in Fig. 1A) along their lengths. A soft silicone

[1]Department of Materials Science and Engineering and Frederick Seitz Materials Research Laboratory, University of Illinois at Urbana-Champaign, Urbana, IL 61801, USA. [2]Department of Electrical and Computer Engineering, University of Illinois at Urbana-Champaign, Urbana, IL 61801, USA. [3]Department of Civil and Environmental Engineering and Department of Mechanical Engineering, Center for Engineering and Health, and Skin Disease Research Center, Northwestern University, Evanston, IL 60208, USA. [4]Department of Civil Engineering and Architecture, Zhejiang University, Hangzhou 310058, P.R. China. [5]Department of Materials Science and Engineering, Department of Energy Engineering, Hanyang University, Seoul 133-791, Republic of Korea. [6]Department of Chemistry, University of Illinois at Urbana-Champaign, Urbana, IL 61801, USA. [7]Key Laboratory of Pressure Systems and Safety (MOE), School of Mechanical and Power Engineering, East China University of Science and Technology, Shanghai 200237, P.R. China. [8]Center for Mechanics and Materials, Tsinghua University, Beijing 100084, P.R. China. [9]Beckman Institute for Advanced Science and Technology, University of Illinois at Urbana-Champaign, Urbana, IL 61801, USA.
*These authors contributed equally to this work. †Corresponding author. E-mail: jrogers@illinois.edu (J.A.R.); y-huang@northwestern.edu (Y.H.); yihui.zhang2011@gmail.com (Y.Z.)
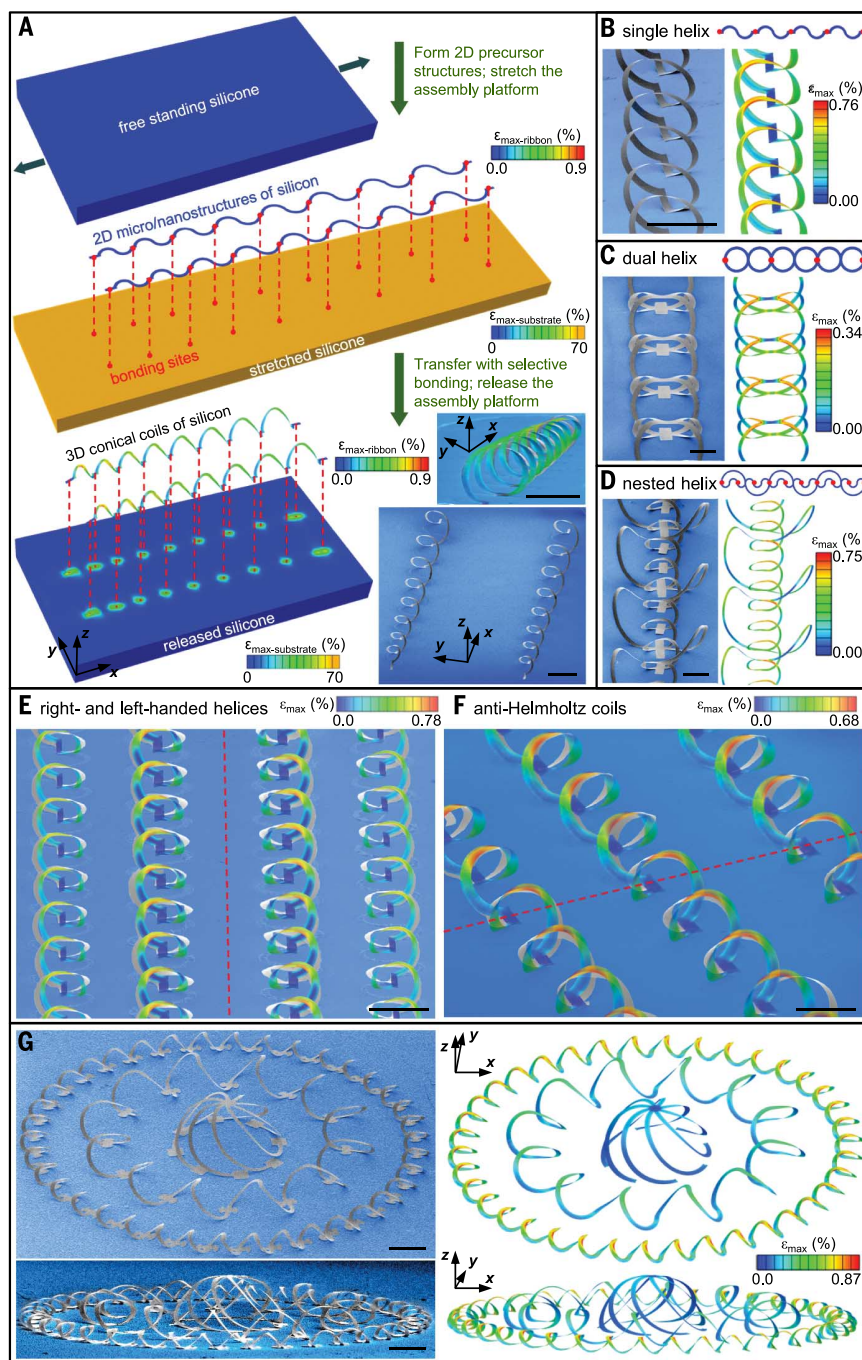
Fig. 1. Process for deterministic assembly of 3D mesostructures of monocrystalline silicon from 2D precursors. (**A**) Finite-element analysis (FEA) results that correspond to the formation of 3D conical helices from 2D filamentary serpentine ribbons of silicon bonded at selected points (red dots) to a stretched slab of silicone elastomer. Compressive forces induced by relaxing the strain in the elastomer lead to coordinated out-of-plane buckling, twisting, and translational motions in the silicon, yielding 3D mesostructures. The scanning electron microscope (SEM) images at the lower right show an experimental result. (**B**) Schematic diagram of a 2D silicon precursor and its bonding sites (top), an SEM image of a single-helical coil formed from this precursor (left), and corresponding FEA prediction (right). (**C** and **D**) Similar results for a dual-helix coil (C) and a nested, coaxial pair of connected helical coils (D). (**E**) SEM image with overlaid FEA prediction of helical coils with right- and left-handed chirality, on the left and right sides of the dashed red line, respectively. (**F**) SEM image with overlaid FEA prediction of structures whose chirality changes abruptly at the locations defined by the dashed red line. (**G**) SEM images and FEA predictions of a complex 3D mesostructure formed from a 2D precursor that consists of closed-loop circular filamentary serpentines and radially oriented ribbons, selectively bonded to a biaxially stretched elastomer substrate. In all cases, the color in the FEA results corresponds to the maximum principal strains. Scale bars, 400 μm.

elastomer substrate (Dragon Skin; Smooth-On, Easton, PA) that is uniaxially stretched to a large level of prestrain ($\varepsilon_{pre} = \Delta L/L$, where ΔL is the increase in length and is comparable to or larger than L; $\varepsilon_{pre} \approx 70\%$ for the case shown here) and is then exposed to ozone to generate a uniform coverage of surface hydroxyl groups serves as a platform that guides the mechanical assembly process. Transfer printing of the 2D serpentines onto this surface leads to strong, spatially selective bonding [work of adhesion >8 J/m^2 (*33*)] via covalent linkages that form upon contact as a result of condensation reactions at the regions of the silicon that present hydroxyl groups (*34, 35*). Comparatively weak van der Waals forces dominate interfacial interactions at all other locations [work of adhesion ~0.2 J/m^2 (*36*)].

Allowing the substrate to return to its original shape induces large compressive forces on the serpentine precursors. Forces above a certain threshold initiate a controlled buckling process that lifts the weakly bonded regions of the serpentines out of contact with the substrate surface and, at the same time, induces spatially dependent deformations (in terms of twisting and bending) and in- and out-of-plane translations. The 3D structures involve a balance between the forces of adhesion to the substrate and the strain energies of the bent, twisted ribbons. The latter (W_{strain}) depends on the elastic modulus (E) and the thickness (t) and lateral dimension (w) of the ribbons via a simple scaling law, $W_{strain} \propto Ewt^3$. The 3D structures formed by these correlated motions represent self-supporting frameworks that remain tethered to the assembly platform at the covalent bonding sites. This process leaves residual strains in the substrate that are negligible everywhere except for the immediate vicinity of these sites, as well as strains in the silicon that are well below fracture thresholds (Fig. 1A). This mechanically guided, deterministic process of geometric transformation from 2D to 3D is governed by (i) the 2D layout of the precursor materials, their dimensions and mechanical properties; (ii) the pattern of sites for selective bonding; and (iii) the nature and magnitude of the prestrain in the assembly platform. The resulting 3D structures differ qualitatively from surface buckling or wrinkling patterns that can occur in thin films [e.g., (*37–39*)]. Quantitative analysis captures all of these aspects, as illustrated by the excellent agreement between experiment and computation in Fig. 1A and fig. S1. The coils shown here have eight turns, with a pitch (i.e., dimension along x axis) that varies gradually from ~454 μm to ~817 μm, a width (i.e., dimension along y axis) from ~252 μm to ~474 μm, and a height (i.e., dimension along z axis) from ~240 μm to ~459 μm. The relative differences between the experimentally observed structural geometries and those from FEA predictions are <8.5%. See (*33*) and figs. S2 and S3 for detailed materials and fabrication procedures.

With this scheme, diverse feature sizes and wide-ranging geometries can be realized in many different classes of materials. A simple case related to that in Fig. 1A results from a precursor that

consists of a 2D serpentine ribbon in a spatially invariant periodic geometry (2 μm thick, 50 μm wide; schematic top-view illustration in the upper panel of Fig. 1B). Here, selective bonding to an assembly platform that is strained uniaxially to $\varepsilon_{pre} = 90\%$ yields a uniform, single-helical coil (Fig. 1B). The experimental results are in quantitative agreement with FEA (Fig. 1B and fig. S4) and with analytical parametric equations developed by exploring key characteristics of the deformations (33) (fig. S5). Such models establish the relationship between geometric configurations and $\varepsilon_{p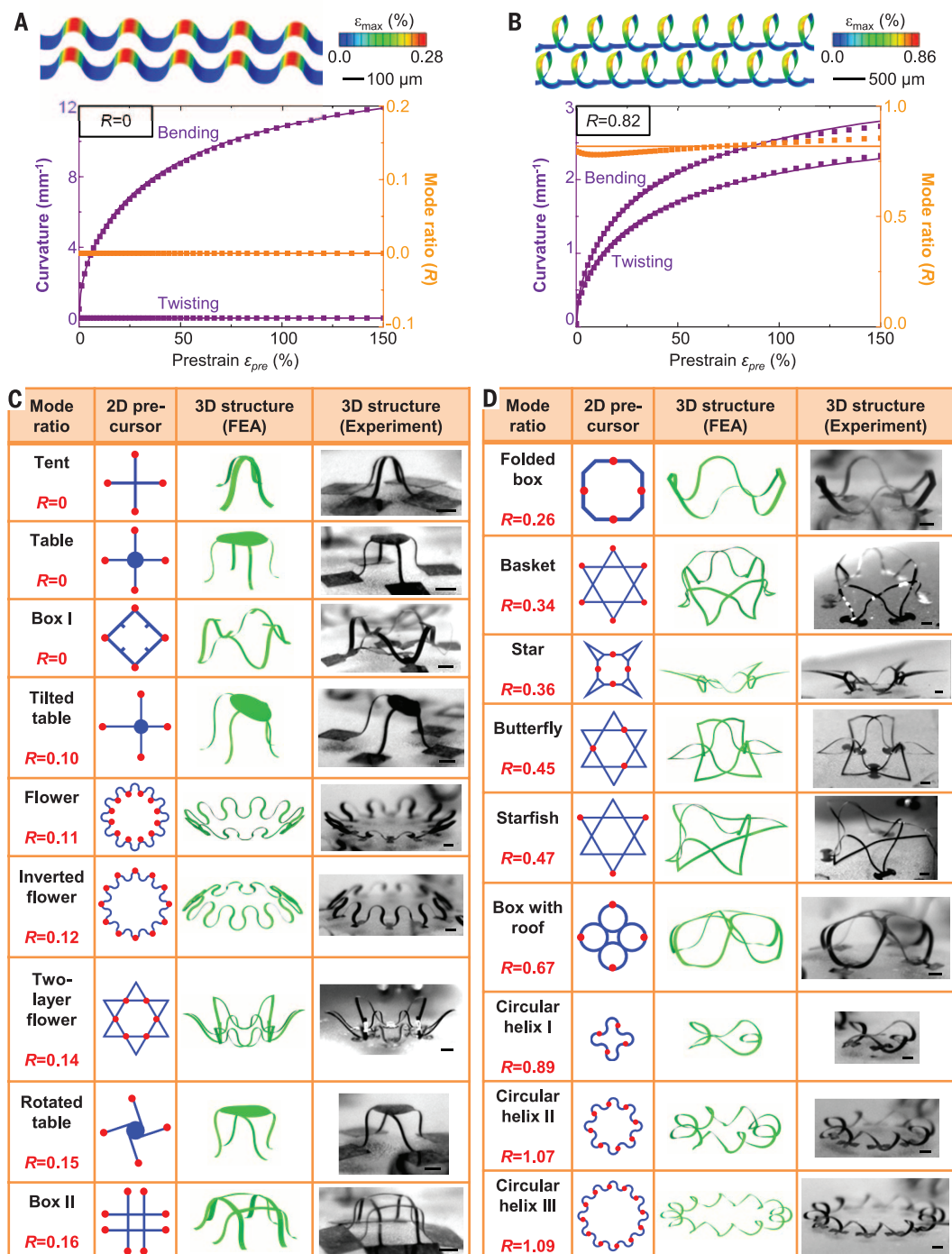re}$, indicating that the heights of the helices increase with ε_{pre} while the widths remain largely unchanged, as might be expected. Modifying the structure of the 2D precursor within this theme while changing the distribution of the bonding sites enables access to dual helices (Fig. 1C), nested coaxial structures (Fig. 1D), helices with opposite chirality (Fig. 1E), and even structures whose chirality changes abruptly at selected locations (Fig. 1F). In all of the examples in Fig. 1, the maximum principal strains in the silicon (from ~0.34% to 0.90%) occur at locations of large changes in curvature. Computational models provide quantitative guidance in the selection of designs that avoid strains at levels that could result in fracture of the constituent materials, localized deformation, or self-contact. For simple cases, some of these guidelines can be captured in analytical forms (33) (fig. S6). In single helices, the maximum strains increase linearly with both the thicknesses and widths of the 2D precursors, with greater sensitivity to the thickness.

The assembled structures are not restricted to geometries with axial symmetry. Joining

Fig. 2. Experimental and computational studies of various 3D mesostructures and classification according to their modes of deformation. (A) Average curvature components and mode ratio of a 3D mesostructure (3D wavy ribbon) that involves only bending, as a function of prestrain in the stretched assembly platform. (B) Similar results for a 3D mesostructure (3D single-helical coil) that involves both bending and twisting. Dots represent FEA results; solid lines represent the scaling law $\kappa_{bend}, \kappa_{twist} \propto \sqrt{\varepsilon_{compr}}$. The colors in the 3D FEA correspond to the maximum principal strains. (C and D) 2D precursors, mode ratios, optical micrographs, and FEA predictions for 18 3D mesostructures that exhibit bending-dominated modes (C) and bending-twisting mixed modes (D). Scale bars, 200 μm.

Mode ratio	2D precursor	3D structure (FEA)	3D structure (Experiment)
Tent R=0			
Table R=0			
Box I R=0			
Tilted table R=0.10			
Flower R=0.11			
Inverted flower R=0.12			
Two-layer flower R=0.14			
Rotated table R=0.15			
Box II R=0.16			

Mode ratio	2D precursor	3D structure (FEA)	3D structure (Experiment)
Folded box R=0.26			
Basket R=0.34			
Star R=0.36			
Butterfly R=0.45			
Starfish R=0.47			
Box with roof R=0.67			
Circular helix I R=0.89			
Circular helix II R=1.07			
Circular helix III R=1.09			

closed-form circular 2D serpentines with equally biaxially stretched assembly platforms (fig. S7) yields toroidal coils in isolation, in extended arrays, or in nested configurations. Figure 1G shows an elaborate 3D silicon mesostructure that consists of a concentric pair of toroids, with a separate hemispherical "cage" construct at the center; the corresponding 2D precursor is shown in fig. S8. The remarkably good agreement be-

tween experimental results and FEA predictions for this highly complex architecture provides further evidence of the fidelity of the assembly process and the accuracy of the models. The result is a deterministic route to 3D mesostructures with validated design tools that can assist in the selection of 2D precursor geometries, bonding sites, and stretching configurations for wide-ranging classes of topologies and architectures.

Dozens of basic 3D shapes, each identified with a descriptive name, are summarized in Fig. 2. A quantitative classification scheme follows from consideration of the buckling characteristics. In general, motions of ribbon-type precursors (i.e., thickness t much smaller than width w) are dominated by out-of-plane bending and twisting deformations coupled with large-scale translational motion (fig. S9). By comparison, in-plane bending is energetically unfavorable because the corresponding stiffness ($\propto w^3t$) is much larger than that for out-of-plane bending or twisting ($\propto wt^3$). The magnitudes of bending and twisting deformations can be quantified by evaluating curvatures that are defined using a local coordinate system (fig. S9). The bending and torsional degrees of freedom of these developable ribbons are constrained by the isometric nature of the deformations (i.e., length invariant, as measured along the central axes of the ribbons) associated with formation of the 3D structures.

Buckling always involves considerable bending, whereas the amount of twisting depends strongly on the 2D structural details. One means of classification relies on a quantity, R, defined by the ratio of the average twisting curvature (κ_{twist}) to the average bending curvature (κ_{bend}), which can be determined by FEA (33). A given 3D mesostructure belongs to the bending-dominated mode when R, referred to as the mode ratio, is smaller than a critical value (e.g., 0.2 for the present purposes); otherwise, it belongs to the bending-twisting mixed mode. Representative examples presented in Fig. 2, A and B, fall into these two different regimes: a 3D wavy ribbon ($R = 0$) and a 3D helical coil ($R = 0.82$). The magnitudes of both κ_{twist} and κ_{bend} increase with compressive strain (ε_{compr}) applied to the 2D precursor, where $\varepsilon_{compr} = \varepsilon_{pre}/(1 + \varepsilon_{pre})$. Quantitative analyses show that both curvature components scale with the square root of ε_{compr}, thereby suggesting that R is independent of the compression level. This finding applies to all of the 3D mesostructures examined here, obtained with a diverse set of topologies and formed on assembly platforms with uniaxial as well as biaxial strains (Fig. 2, A and B, and figs. S10 and S11).

The layout of the 2D precursor and the configuration of the bonding sites both play crucial roles in determining the final 3D geometry (Fig. 2, C and D). With the same 2D precursor (e.g., the circular serpentine pattern or Kagome lattice), different distributions of bonding sites yield different 3D configurations, with widely varying values of R. By comparison to these two factors, the cross-sectional dimensions (i.e., w and t) of the precursor have minor effect. For 3D mesostructures that exhibit a bending-dominated mode (e.g., the flower and two-layer flower of Fig. 2C), R is insensitive to changes in the width or thickness (fig. S12). For bending-twisting mixed modes (e.g., straight helix in Fig. 1B and circular helix III in Fig. 2D), the width and thickness can lead to changes in R, but with magnitudes insufficient to induce a transition into the bending-dominated mode.

Multiple, hierarchical scales of buckling are also possible with the appropriate choice of design.
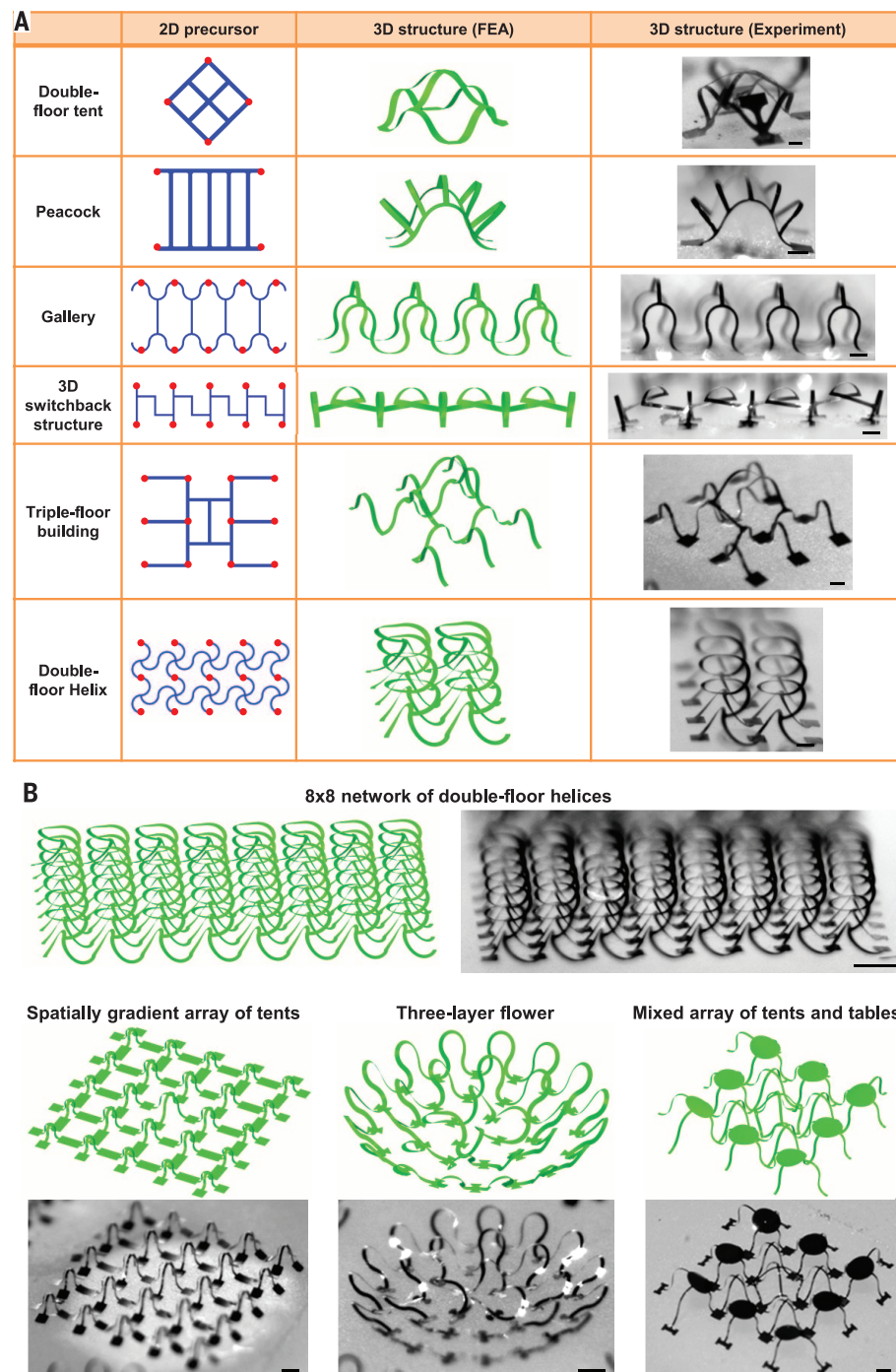

Fig. 3. 3D mesostructures with multilevel configurations and/or extended network architectures. (**A**) 2D precursors, FEA predictions, and optical micrographs for six 3D mesostructures that have double- or triple-level configurations. (**B**) Distributed 3D mesoscale networks comprising interconnected collections of the 3D structures in Figs. 2 and 3A. Scale bars, 200 μm (A), 400 μm (B).

Examples of 3D mesostructures that have multi-level constructions in the out-of-plane direction are presented in Fig. 3A. Such layouts can be achieved by adding filamentary ribbons to 2D precursors that yield single-level 3D shapes like those of Fig. 2. In the most extreme examples, these additional ribbons connect the precursor structures together at regions where the assembly process would otherwise yield the maximum out-of-plane displacements. Upon release of strain in the assembly platform, these ribbons—such as those that form the cross in the double-floor tent structure, the array of vertical ribbons in the peacock and gallery structures, or the horizontally aligned serpentine ribbons in the double-floor helix structure—undergo an additional level of buckling to form an elevated "second floor" suspended above the reach of buckling that represents the "first floor." This process substantially extends the maximum elevation above the substrate, thereby enhancing the 3D nature of the system. The triple-floor building structure provides a specific example. Here, the maximum out-of-plane displacement is ~1 mm for assembly using a biaxial prestrain of ~100%. This distance is up to ~2 times the maximum in-plane extent along the narrow dimension of the central part of the supporting structure.

The 3D mesostructures shown in Figs. 2 and 3A can be viewed as building blocks to yield large-scale, interconnected 3D mesoscale networks. The examples in Fig. 3B follow from repeating, mixing, joining, and/or nesting of these building blocks. The top frame shows an 8 × 8 array of the double-floor helix structure that consists of eight evenly spaced helices on the first floor and another eight helices, with the axial direction rotated by 90°, on the second floor (fig. S13). The lower left panel of Fig. 3B illustrates a 5 × 5 array of the 3D tent structure with a spatial gradient in the height, such that the largest tent appears at the center and smaller ones reside at the outermost peripheral regions. To its right is a dual, nested 3D flower structure with a fourfold symmetric toroid at the center. The rightmost example corresponds to a mixed array consisting of four regular table structures, four tilted tables, four tents, and one double-floor tent at the center. Some other 3D mesostructures (e.g., raised ring, scaffold, toroid inside a flower, nested box, etc.) appear in fig. S14. These networks exhibit geometries that agree quantitatively with FEA predictions. An important point is that all 3D mesostructures—even those with the highest complexity and largest extent in the out-of-plane direction—are deterministic and form consistently into unique geometries because the strain energies of the first-order buckling modes (i.e., energetically the most probable configuration) are lower than those of all other modes by approximately a factor of 2 or more (fig. S15).

Summarized in Fig. 4A and fig. S16 are results that illustrate the applicability of this assembly approach to additional classes of materials, including metals (e.g., Ni), dielectrics (e.g., polyimide and epoxy), and patterned combinations

of these, in polycrystalline and amorphous forms. Submicrometer features are also possible, as demonstrated in a "starfish" framework that incorporates silicon ribbons with widths of 800 nm and thicknesses of 100 nm (Fig. 4B). Two more examples of submicrometer features are provided in fig. S17. Here, the large differences in contact areas between the filaments and the bonding sites provide the necessary contrast in adhesion. The same strategy also enables the assembly of micrometer-sized 3D silicon features with ribbon widths of 3 μm and thicknesses of 300 nm (fig. S18). In these and all

other cases, mechanical strain applied to the assembly platforms can affect reversible, controlled changes in the geometries of the supported structures, thereby providing tunable 3D configurations. The results in Fig. 4C show top and angled views of the influence of uniaxial tensile deformation (50%) on a structure with a variant of the starfish layout, in which all six tip corners serve as sites for bonding. Overlaid FEA results exhibit quantitative agreement with the observed geometries. Results in fig. S19 demonstrate that the 3D mesostructures are bendable and can be placed on curved surfaces.
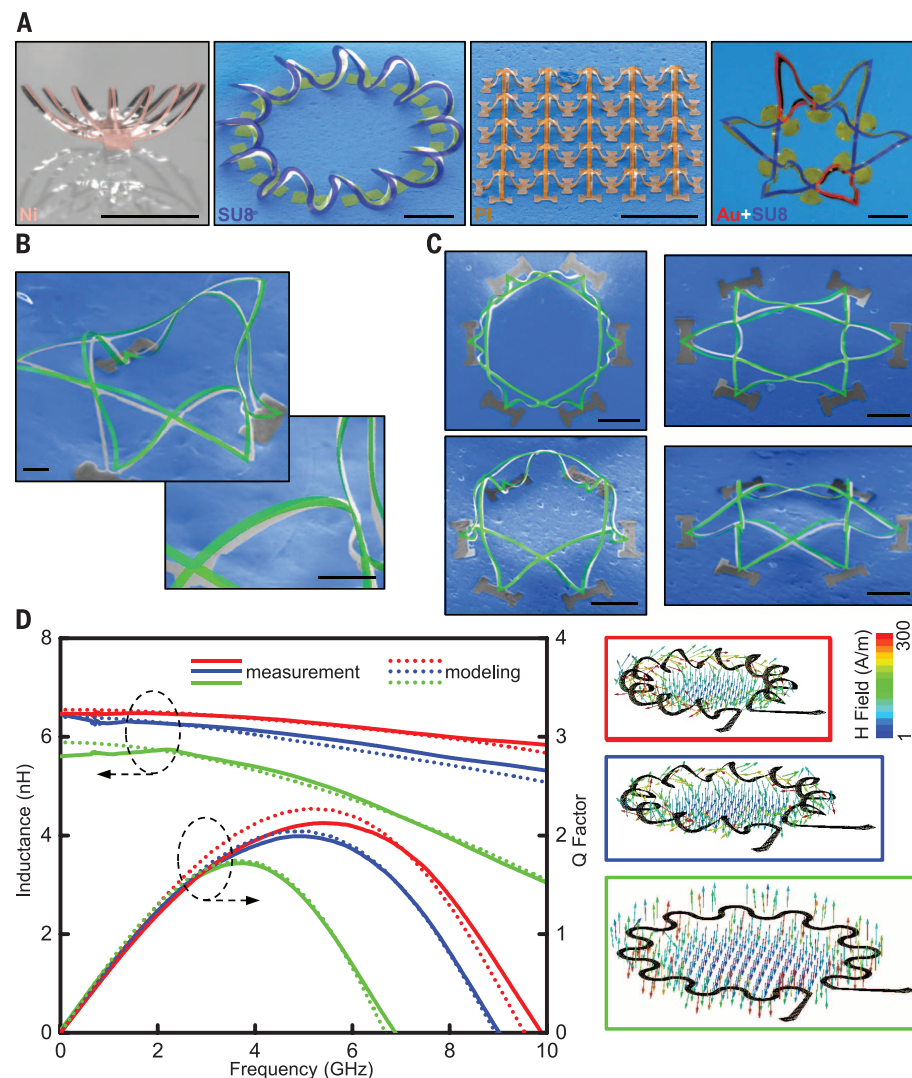

Fig. 4. 3D structures with various material compositions and feature sizes, and results for electrical behaviors in a tunable 3D toroidal inductor. (A) Experimental images and overlaid FEA predictions of 3D mesostructures made of metal (Ni), polymer [photodefinable epoxy (SU8) and polyimide (PI)], and heterogeneous combinations of materials (Au and SU8). Scale bars, 500 μm. (B) 3D mesostructures of silicon with lateral dimensions and thicknesses in the submicrometer regime, with overlaid FEA predictions. Scale bars, 5 μm. (C) 3D mesostructure of silicon in its as-fabricated state (left column) and in a configuration that results from uniaxially stretching the substrate (right column), all with overlaid FEA predictions. Scale bars, 50 μm. (D) Measured and computed frequency dependence of the inductance and the Q factor of a single 3D toroidal inductor mechanically configured into two different shapes by partial (21%, in an absolute sense, of an original prestrain of 54%; blue) and then complete release of prestrain (red), along with the corresponding 2D precursor (green) as reference. The panels on the right show simulated magnetic field distributions of these structures for feed-in power of 1 W. The arrows indicate direction and their colors indicate magnitude.

The ability to naturally integrate state-of-the-art electronic materials and devices represents an essential, defining characteristic of these approaches. A mechanically tunable inductor based on a 3D toroidal structure with feed and ground lines, all constructed with polyimide encapsulation (1.2 μm) and Ni conducting layers (400 nm), provides an example. Here, the geometry is similar to the "circular helix III" in Fig. 2D, with the addition of contact pads located at the periphery for electrical probing. The graph of Fig. 4D shows measurements and modeling results for the frequency dependence of the inductance and the quality (Q) factor for a 2D closed-loop serpentine precursor and a single 3D toroid structure in two different mechanically adjusted configurations. In both cases, the 3D cage structure enhances the mutual inductance between adjacent twisted turns. The maximum Q factors and resonant frequencies increase systematically from 1.7 to 2.2 GHz and from 6.8 to 9.5 GHz, respectively, as the structure transforms from 2D to two distinct 3D shapes associated with partial release (about half of the total initial prestrain of 54%) and then complete release of the prestrain. These trends arise from a systematic reduction in substrate parasitic capacitance with increasing three-dimensional character (40). The measured results correspond well to modeling that involves computation of the electromagnetic properties associated with the predicted 3D structure geometries from FEA, as shown in the right panels of Fig. 4D [see (33) and figs. S20 to S23].

The ideas presented here combine precise, lithographic control of the thicknesses, widths, and layouts of 2D structures with patterned sites of adhesion to the surfaces of high-elongation elastomer substrates to enable rapid assembly of broad classes of 3D mesostructures of relevance to diverse microsystem technologies. The process, which can be implemented with any substrate that is capable of controlled, large-scale dimensional change, expands and complements the capabilities of other approaches in 3D materials assembly. Compatibility with the most advanced materials (e.g., monocrystalline inorganics), fabrication methods (e.g., photolithography), and processing techniques (e.g., etching, deposition) that are available in the semiconductor and photonics industries suggest many possibilities for achieving sophisticated classes of 3D electronic, optoelectronic, and electromagnetic devices.

REFERENCES AND NOTES

1. V. B. Shenoy, D. H. Gracias, MRS Bull. 37, 847–854 (2012).
2. F. Li, D. P. Josephson, A. Stein, Angew. Chem. Int. Ed. 50, 360–388 (2011).
3. N. B. Crane, O. Onen, J. Carballo, Q. Ni, R. Guldiken, Microfluid. Nanofluid. 14, 383–419 (2013).
4. J. H. Jang et al., Adv. Funct. Mater. 17, 3027–3041 (2007).
5. J. Fischer, M. Wegener, Laser Photonics Rev. 7, 22–44 (2013).
6. K. A. Arpin et al., Adv. Mater. 22, 1084–1101 (2010).
7. W. L. Noorduin, A. Grinthal, L. Mahadevan, J. Aizenberg, Science 340, 832–837 (2013).
8. P. X. Gao et al., Science 309, 1700–1704 (2005).
9. M. Huang, F. Cavallo, F. Liu, M. G. Lagally, Nanoscale 3, 96–120 (2011).
10. H. Tian et al., Nat. Mater. 11, 986–994 (2012).
11. T. G. Leong et al., Proc. Natl. Acad. Sci. U.S.A. 106, 703–708 (2009).
12. M. Yu et al., ACS Nano 5, 2447–2457 (2011).
13. D. Bishop, F. Pardo, C. Bolle, R. Giles, V. Aksyuk, J. Low Temp. Phys. 169, 386–399 (2012).
14. R. J. Wood, Am. Sci. 102, 124–131 (2014).
15. R. Songmuang, A. Rastelli, S. Mendach, O. G. Schmidt, Appl. Phys. Lett. 90, 091905 (2007).
16. J. H. Lee et al., Adv. Mater. 26, 532–569 (2014).
17. M. Schumann, T. Buckmann, N. Gruhler, M. Wegener, W. Pernice, Light Sci. Appl. 3, e175 (2014).
18. X. Zheng et al., Science 344, 1373–1377 (2014).
19. T. A. Schaedler et al., Science 334, 962–965 (2011).
20. C. M. Soukoulis, M. Wegener, Nat. Photonics 5, 523–530 (2011).
21. J. H. Cho et al., Small 7, 1943–1948 (2011).
22. B. Y. Ahn et al., Science 323, 1590–1593 (2009).
23. W. Huang et al., Nano Lett. 12, 6283–6288 (2012).
24. H. Zhang, X. Yu, P. V. Braun, Nat. Nanotechnol. 6, 277–281 (2011).
25. K. Sun et al., Adv. Mater. 25, 4539–4543 (2013).
26. W. Zheng, H. O. Jacobs, Adv. Funct. Mater. 15, 732–738 (2005).
27. X. Guo et al., Proc. Natl. Acad. Sci. U.S.A. 106, 20149–20154 (2009).
28. V. Y. Prinz et al., Physica E 6, 828–831 (2000).
29. O. G. Schmidt, K. Eberl, Nature 410, 168–168 (2001).
30. L. Zhang et al., Microelectron. Eng. 83, 1237–1240 (2006).
31. G. Hwang et al., Nano Lett. 9, 554–561 (2009).
32. W. Gao et al., Nano Lett. 14, 305–310 (2014).
33. See supplementary materials on Science Online.
34. D. C. Duffy, J. C. McDonald, O. J. A. Schueller, G. M. Whitesides, Anal. Chem. 70, 4974–4984 (1998).
35. Y. Sun, W. M. Choi, H. Jiang, Y. Y. Huang, J. A. Rogers, Nat. Nanotechnol. 1, 201–207 (2006).
36. D. H. Kim et al., Science 333, 838–843 (2011).
37. S. Yang, K. Khare, P. C. Lin, Adv. Funct. Mater. 20, 2550–2564 (2010).
38. S. Singamaneni, V. V. Tsukruk, Soft Matter 6, 5681–5692 (2010).
39. D. H. Kim, N. S. Lu, Y. G. Huang, J. A. Rogers, MRS Bull. 37, 226–235 (2012).
40. C. P. Yue, S. S. Wong, IEEE Trans. Electron. Dev. 47, 560–568 (2000).

BIOMATERIALS

Electronic dura mater for long-term multimodal neural interfaces

Ivan R. Minev,[1]* Pavel Musienko,[2,3]* Arthur Hirsch,[1] Quentin Barraud,[2] Nikolaus Wenger,[2] Eduardo Martin Moraud,[4] Jérôme Gandar,[2] Marco Capogrosso,[4] Tomislav Milekovic,[2] Léonie Asboth,[2] Rafael Fajardo Torres,[2] Nicolas Vachicouras,[1,2] Qihan Liu,[5] Natalia Pavlova,[2,3] Simone Duis,[2] Alexandre Larmagnac,[6] Janos Vörös,[6] Silvestro Micera,[4,7] Zhigang Suo,[5] Grégoire Courtine,[2]†‡ Stéphanie P. Lacour[1]†‡

The mechanical mismatch between soft neural tissues and stiff neural implants hinders the long-term performance of implantable neuroprostheses. Here, we designed and fabricated soft neural implants with the shape and elasticity of dura mater, the protective membrane of the brain and spinal cord. The electronic dura mater, which we call e-dura, embeds interconnects, electrodes, and chemotrodes that sustain millions of mechanical stretch cycles, electrical stimulation pulses, and chemical injections. These integrated modalities enable multiple neuroprosthetic applications. The soft implants extracted cortical states in freely behaving animals for brain-machine interface and delivered electrochemical spinal neuromodulation that restored locomotion after paralyzing spinal cord injury.

Implantable neuroprostheses are engineered systems designed to study and treat the injured nervous system. Cochlear implants restore hearing in deaf children, deep brain stimulation alleviates Parkinsonian symptoms, and spinal cord neuromodulation attenuates chronic neuropathic pain (1). New methods for recording and modulation of neural activity using electrical, chemical, and/or optical modalities open promising therapeutic perspectives for neuroprosthetic treatments. These advances have triggered the development of myriad neural technologies to design multimodal neural implants (2–5). However, the conversion of these sophisticated technologies into implants mediating long-lasting therapeutic benefits has yet to be achieved. A recurring challenge restricting long-term biointegration is the substantial biomechanical mismatch between implants and neural tissues (6–8).

Neural tissues are viscoelastic (9, 10) with elastic and shear moduli in the 100- to 1500-kPa range. They are mechanically heterogeneous (11, 12) and endure constant body dynamics (13, 14). In contrast, most electrode implants—even thin, plastic interfaces—present high elastic moduli in the gigapascal range, thus are rigid compared to neural tissues (3, 15). Consequently, their surgical insertion triggers both acute and long-term tissue responses (6–8, 14). Here, we tested the hypothesis that neural implants with mechanical properties matching the statics and dynamics of host tissues will display long-term biointegration and functionality within the brain and spinal cord.

We designed and engineered soft neural interfaces that mimic the shape and mechanical behavior of the dura mater (Fig. 1, A and B, and fig. S1). The implant, which we called electronic dura mater or e-dura, integrates a transparent silicone

Assembly of micro/nanomaterials into complex, three-dimensional architectures by compressive buckling

Sheng Xu, Zheng Yan, Kyung-In Jang, Wen Huang, Haoran Fu, Jeonghyun Kim, Zijun Wei, Matthew Flavin, Joselle McCracken, Renhan Wang, Adina Badea, Yuhao Liu, Dongqing Xiao, Guoyan Zhou, Jungwoo Lee, Ha Uk Chung, Huanyu Cheng, Wen Ren, Anthony Banks, Xiuling Li, Ungyu Paik, Ralph G. Nuzzo, Yonggang Huang, Yihui Zhang, and John A. Rogers

Popping materials and devices from 2D into 3D

Curved, thin, flexible complex three-dimensional (3D) structures can be very hard to manufacture at small length scales. Xu *et al.* develop an ingenious design strategy for the microfabrication of complex geometric 3D mesostructures that derive from the out-of-plane buckling of an originally planar structural layout (see the Perspective by Ye and Tsukruk). Finite element analysis of the mechanics makes it possible to design the two 2D patterns, which is then attached to a previously strained substrate at a number of points. Relaxing of the substrate causes the patterned material to bend and buckle, leading to its 3D shape.

Science, this issue p. 154; see also p. 130

View the article online
https://www.science.org/doi/10.1126/science.1260960
Permissions
https://www.science.org/help/reprints-and-permissions

Use of this article is subject to the Terms of service